Molecular analog of perovskite ferrites: First-principles studies of electronic and magnetic properties

Mian Wang, Tianyi Wang, Minhui Yuan, Qian Zhang, Shenghua Liu, Jing Shuai, and Xiang-Guo Li*
School of Materials, Sun Yat-sen University, Shenzhen 518107, China

(Received 28 April 2023; revised 11 September 2023; accepted 2 November 2023; published 21 November 2023)

The recently synthesized molecular compound $[Ce_2^{III}Ce^{IV}Mn_8^{III}O_8(O_2CPh)_{18}(HO_2CPh)]$ (Ce_3Mn_8) has gained much interest due to its structural resemblance to the repeating unit of perovskite manganites and containing rich physics. We investigate the electronic and magnetic properties of the molecular analog of perovskite ferrites $[Ce_2^{III}Ce^{IV}Fe_8^{III}O_8(O_2CPh)_{18}(HO_2CPh)]$ (Ce_3Fe_8), another fascinating family of magnetic oxides, using first-principles methods. Our results have shown that compared to Mn^{III}, the inclusion of the $d_{x^2-y^2}$ orbital in Fe^{III} can exhibit a strong antiferromagnetic (AF) Fe-O-Fe superexchange interaction and a pronounced asymmetric behavior of the Fe-Ce-Fe ferromagnetic (FM) interaction involving the central Ce-f orbitals. The combination of pairwise Fe_2^{III} FM and AF exchange interactions result in C-type AF spin vector alignments that are found within the 3-D perovskites but are different from Ce_3Mn_8. The Wannier orbital analysis indicates that the edge Ce-f orbitals, though farther away from the Fermi level, can hybridize with the central Ce-f orbitals near the Fermi level, giving rise to a FM interaction between the neighboring Fe ions with relatively large distance. These findings can contribute to the theory of magnetism in complex magnetic molecules involving mixed valence and both d and f electrons.

DOI: 10.1103/PhysRevB.108.184421

I. INTRODUCTION

Magnetic perovskite materials continue to attract widespread attention in the scientific community due to their excellent and fascinating physical properties such as colossal magnetoresistance and multiferroicity [1–6]. These materials have been supported for use in multiple applications in the technology fields, such as energy transfer and information storage [7–9]. While the investigation of the underlying mechanisms in such materials is often limited by their complex nature [10], a molecular bottom-up approach to making 0-D species, which are fragments of the bulk 3-D materials, can overcome the limitations and complexities in the synthesis and characterization of bulk 3-D materials [11,12]. Compared with 3-D solids, the 0-D molecules with stable organic ligand shells exhibit more important and advanced properties. The significant competitiveness for such advantages of molecules in the area of known physical phenomena, and the discovery of new ones, is well documented in the field of single-molecule magnets [13–15]. A molecule of the perovskite manganite repeating units $[Ce_2^{III}Ce^{IV}Mn_8^{III}O_8(O_2CPh)_{18}(HO_2CPh)]$, abbreviated as Ce_3Mn_8, was successfully synthesized previously [16]. The combination of experimental and theoretical study [16] reveals that the spin-ordered state of the Ce_3Mn_8 molecule is the same as that in the 3-D C-type antiferromagnetic perovskites, and the mixes of $+3/+4$ oxidation states of Ce ions make the molecule one of the few $3d$-$4f$ complexes and exhibit Mn-Ce-Mn direct magnetic exchange via $Ce^{IV}-f$ orbitals. The rich and complex magnetic interactions involving both d and f electrons in Ce_3Mn_8 make it valuable for further investigation [17]. In particular, the nanoscale size of the molecule enables the fine-tuning of its properties by chemical doping or external manipulation, which is intrinsically different from its corresponding 3-D bulk perovskite. Cation substitution effects on atomic structure and the charging energy of Ce_3Mn_8 have been investigated using the first-principles method [18]. As proved to possess significant effects on the magnetism of bulk perovskite [19–23], the transition metal (TM) anion substitution of Mn in the molecule also needs further investigation.

Due to the similar ionic radii with Mn, the Fe ion is a good substitution choice to the Mn ion, which will not result in strong structural distortion [22,24]. However, the difference between the electronic structures of Mn and Fe, with one more occupied electron in the $3d$ orbital for Fe, can lead to distinct behavior upon substitutions [19,20]. For example, Varignon *et al.* have demonstrated that different TM elements of B (including Fe and Mn) in ABO_3 perovskites can display completely different geometry and electronic and magnetic properties [19]. Yamaguchi *et al.* have indicated that different TM elements of M (Mn, Fe, Co, and Zn) in $M^{II}-Ln^{III}-M^{II}$ magnetic molecules can exhibit different M-Ln bonding geometries and magnetic coupling strength [25]. Further studies need to be performed to understand the TM substitution effects (for example, Fe substitution of Mn) on the electronic and magnetic properties of the molecular analog of magnetic perovskite materials.

In this work we investigate the electronic and magnetic properties of Ce_3Fe_8, a molecular analog of the perovskite repeating units by replacing Mn ions with Fe ions in Ce_3Mn_8 [16,18], using the first-principles method. Our calculations

*lixguo@mail.sysu.edu.cn

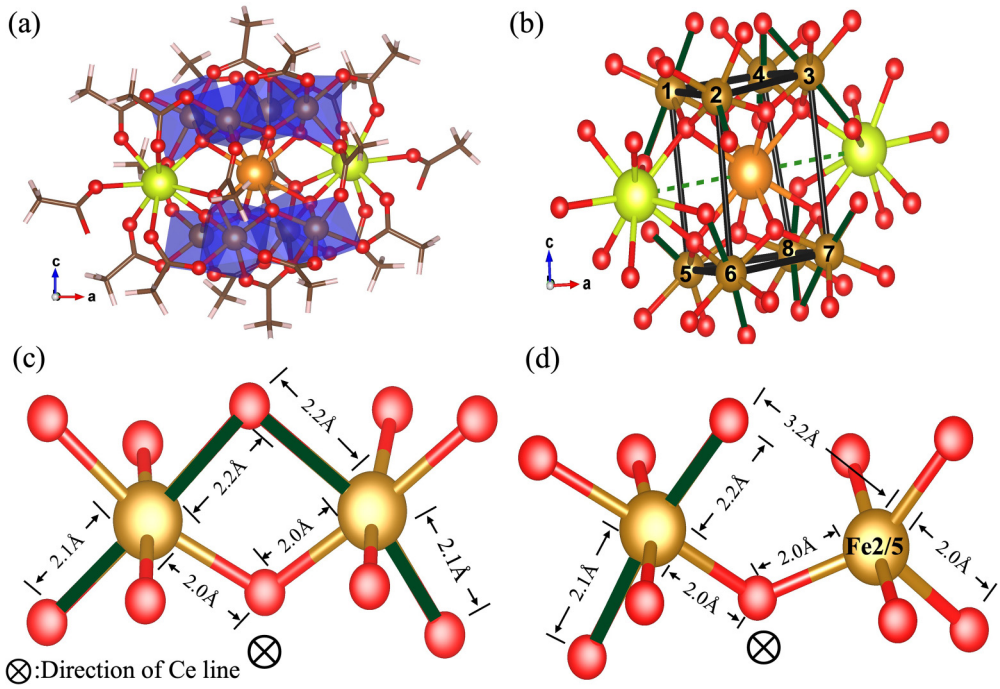

FIG. 1. The optimized molecular structure of Ce_3Fe_8. (a) The complete molecular structure of Ce_3Fe_8 with -CH_3 as the ligand group. The FeO_6 octahedra (FeO_5 pentahedron) are shaded in blue. Color scheme: Ce^{IV} orange; Ce^{III} green; Fe^{III} brown; O red. (b) The partial Ce_3Fe_8 central fragment without ligands, showing only the Ce-O and Fe-O bonds. The Jahn-Teller axes are marked with thicker Fe-O bonds. The Ce line is denoted by a dotted line. The Fe curb is labeled by black line. (c) The structure of Jahn-Teller axes in FeO_6; the Fe-O bonds are 2.1 Å ∼ 2.2 Å, longer than the other Fe-O bonds which are 2.0 Å, not shown. (d) The Jahn-Teller axes of FeO_6 and FeO_5; the bridging oxygen is close to Fe ion within FeO_6, while the distance of bridging oxygen and Fe ion within FeO_5 is 3.2 Å. Direction of Ce line is indicated in the figure.

show that differently from Ce_3Mn_8, the exchange coupling via Fe-$d_{x^2-y^2}$ orbitals can lead to an antiferromagnetic (AF) Fe-O-Fe superexchange coupling and a pronounced anisotropic Fe-Ce-Fe ferromagnetic (FM) interaction. In addition, some of the Fe-O-Fe FM exchange paths between neighboring Fe ions will be destroyed or weakened in Ce_3Fe_8 due to the increased Fe-O distance, further strengthening the AF interaction between neighboring Fe ions. The total energy calculations indicate that the Ce_3Fe_8 molecule has a ground state of *C*-type AF (C-AF-2 in Fig. 2), in contrast to the *C*-type (C-AF-1 in Fig. 2) AF ground state in Ce_3Mn_8. The density functional theory (DFT) Wannier function analysis reveals that the edge Ce-f orbitals, in particular the f_{z^3}, $f_{x(x^2-3y^2)}$, and $f_{y(y^2-3x^2)}$ orbitals, can hybridize with the central Ce-f orbitals that are close to the Fermi level, and thus contribute a sizable FM interaction between neighboring Fe ions. Our results confirm the existence of metal-to-metal FM coupling involving f electrons, the strength of which strongly depends on the shape and energy level positions of the hybridized orbitals.

II. METHOD

Our first-principles calculations are carried out within the framework of Kohn-Sham DFT [26] with the generalized gradient corrected Perdew-Burke-Ernzerhof (PBE) exchange-correlation functional [27] using the Vienna *Ab initio* Simulation Package (VASP) code [28,29]. The electron-ion interaction was described using projector augmented wave (PAW) potentials [30,31]. The energy cutoff for plane-wave basis expansion was set to 500 eV. The threshold for self-consistency and structure optimization were set to 10^{-5} eV and 0.01 eV/Å, respectively. The molecule was put into a large periodic supercell of 28 Å × 22 Å × 24 Å. The distance between a molecule and its repeating image is larger than 10 Å, so the van der Waals interaction between them was ignored in the calculation. Because of the strong localization of Ce-f and Fe-d orbitals, the GGA+U method proposed by Dudarev *et al.* [32] was applied with $U = 2.0$ eV [16,33] and 4.1 eV [34,35] for the Ce-f electron and Fe-d electron, respectively, in line with previous works [16,36]. As applied in the 3d- and 4f-element perovskite oxides [37–40], we do not consider the spin-flip terms in the corresponding magnetic molecules [41,42]. The Wannier90 package [43] was applied to calculate Wannier functions. The spin-orbit couplings (SOCs) were also included. We find SOC has negligible effects on the exchange couplings (see results section), consistent with previous works on transition metal perovskite oxides involving 3d and 4f elements [44,45]. Thus we will focus on the *LS* coupling or the Russell-Saunders regime in this work [41,42], while we want to emphasize that there are still some open questions about the relative strengths of the different microscopic mechanisms, which could only be conclusively resolved once a relevant experiment is performed.

III. RESULTS

A. Atomic structure

The initial structure of the Ce_3Fe_8 molecule is obtained by substituting Fe ions for Mn ions in the recently reported

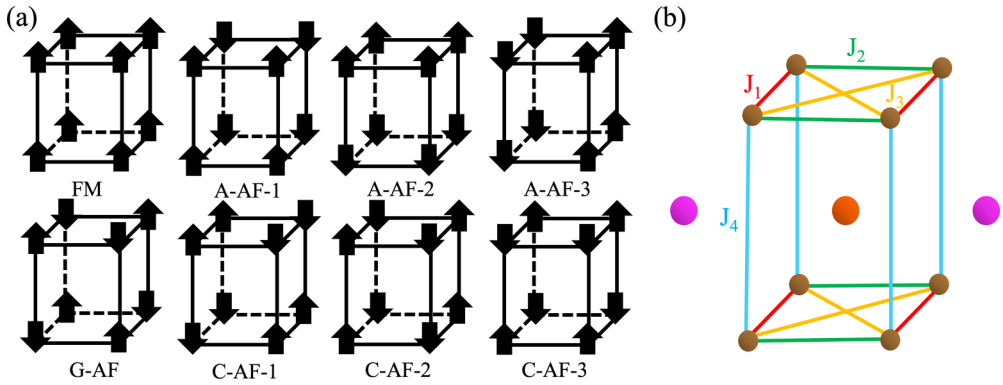

FIG. 2. (a) Eight spin-ordering configurations in a $Ce_3Fe_8^{III}$ molecule, derived from four known configurations in a perovskite unit cell. (b) The multispin Heisenberg model showing the magnetic exchange coupling paths labeled as J_1 to J_4; lines in the same color indicate symmetry-equivalent paths. Other possible paths are unlabeled because of the exchange coupling strengths at least an order of magnitude smaller than the ones labeled in the figure.

Ce_3Mn_8 molecule [16]. In analogy to Ce_3Mn_8, the Ce_3Fe_8 molecule has a striking structural similarity to the repeating unit of perovskite, which resembles a repeating unit of the ABO_3 cubic with distortions plus two A ions, as shown in Figs. 1(a) and 1(b). The core of Ce_3Fe_8 includes eight Fe sites and three Ce sites. Three Ce ions are arranged in a line as shown in Fig. 1(b). The central Ce ion has an oxidation state of +4 and is eight-coordinated, while the other two have an oxidation state of +3 and are nine-coordinated. The eight Fe ions in Ce_3Fe_8 can be divided into two groups; each group has four Fe^{III} ions, which are separated by the Ce line, denoted as the top group (Fe1, Fe2, Fe3, Fe4) and the bottom group (Fe5, Fe6, Fe7, Fe8).

After geometry optimization, significant changes in the atomic structure between Ce_3Fe_8 and Ce_3Mn_8 are observed. Two of the previous eight six-coordinated TMO_6 octahedra located at sites of distorted tetragonal lattice in Ce_3Mn_8 become the FeO_5 pentahedron in Ce_3Fe_8. The remaining six FeO_6 octahedra have Jahn-Teller (JT) distortion, while the two Fe ions (Fe2 and Fe5) with the distorted pentahedron are five-coordinated without JT distortion [46] located in different Fe groups. The FeO_6 octahedra (FeO_5 pentahedron) in different groups share neither corners nor edges across the Ce line, but the neighboring Fe ions from top and bottom, respectively, are connected by a carboxylate group. In both Ce_3Fe_8 and Ce_3Mn_8, along the Ce line direction, the neighboring TMO_6 octahedra within each TM group share one corner with one bridging oxygen atom with TM-O-TM angle greater than 120°, and a carboxylate group connects the two TM ions within these neighboring TMO_6 octahedra, e.g., Fe1/Fe4, Fe2/Fe3, Fe5/Fe8, Fe6/Fe7 in Ce_3Fe_8. For the direction normal to the Ce line, the original two edge-sharing TMO_6 octahedra with two bridging oxygen atoms in Ce_3Mn_8 become corner-sharing with one oxygen atom (Fe1/Fe2 and Fe5/Fe6) due to the transition of octahedra to pentahedron in Ce_3Fe_8. The remaining two neighboring octahedra pairs (Fe3/Fe4 and Fe7/Fe8) in Ce_3Fe_8 are still edge-sharing with two bridging oxygen atoms. The corresponding two TM-O-TM angles are around 83° to 88° and greater than 120°, respectively.

The transition of octahedra to pentahedron in Fe2 and Fe5 is due to the breaking of a Fe-O bond along the previously JT axis, as shown in Figs. 1(c) and 1(d). The bond lengths of Fe-O bonds are usually around 2.1–2.2 Å along the elongated JT axis and about 2.0 Å along the remaining two axes in an octahedron [see Fig. 1(c)], while the Fe-O distances become 3.2 Å and 2.0 Å along the original JT axis in a pentahedron (Fe2 and Fe5) with one Fe-O bond broken and one previous Fe-O elongated bond restoring to a normal bond length without elongation [see Fig. 1(d)]. The two broken Fe-O bonds also result in the transition of the previous two edge-sharing sites with two bridging oxygen atoms to corner-sharing with only one bridging oxygen atom along the direction normal to the Ce line.

B. Magnetic structure and first-principles energetics

According to the empirical Goodenough-Kanamori (GK) rules [47–49], different Fe-Fe pairs can exhibit FM or AF interactions depending on the Fe-O-Fe angles. The combination of FM and AF interactions can result in four known common types of spin-ordering configurations, FM and three kinds of AF: A-AF, C-AF, and G-AF [50]. The eight spin-ordering configurations illustrated in Fig. 2(a) originate from these four spin-ordering configurations after considering all three orientations of the interaction planes (three types of A-AF) or axes (three types of C-AF).

To reveal the magnetic structure of Ce_3Fe_8, we performed DFT calculations for the eight high-symmetry spin-ordering configurations, as shown in Fig. 2(a). This approach based on DFT has been widely used to characterize the magnetic structures of magnetic perovskites [35,51–53]. Table I presents the calculated total energies and atomically resolved magnetic moments for these eight magnetic configurations. The calculation results without considering SOC are also supplied in Supplemental Material [54] Table S1, showing that SOC has little effect on the magnetic exchange coupling in this molecule. Since the experimental structure was applied in the calculations of Ref. [16], we performed additional calculations on the magnetic properties of the Ce_3Mn_8 molecule with DFT relaxed structure (see Supplemental Material [54] Tables S2 and S3), so as to make it comparable with the calculations for the Ce_3Fe_8 molecule in this work. The structure difference between the DFT relaxed and experimental structures can result in sizable exchange coupling strength changes, but

TABLE I. Total energy (E) in meV and magnetic moments (M) in μ_B of Ce_3Fe_8 molecule in different spin-ordered states. "abs" is the absolute value.

Spin order	E	$M_{Ce^{IV}}$	abs(M_{Fe})	M_{Fe}	abs(M_O)	M_O	M_{CH}	M_{total}
FM	716.7	0.05	34.2	34.2	4.29	4.29	0.21	39.89
A-AF-1	382.2	0.02	34.00	0.00	2.98	0.00	0.00	0.00
A-AF-2	726.5	0.02	34.18	0.01	4.09	0.00	0.01	0.00
A-AF-3	303.6	−0.11	33.97	0.02	2.89	0.02	0.00	−0.13
C-AF-1	285.4	−0.06	33.95	0.00	2.78	0.02	0.00	0.00
C-AF-2	0.0	−0.07	33.79	−0.03	1.84	0.04	−0.01	−1.88
C-AF-3	407.9	0.04	33.99	0.09	2.85	−0.05	0.01	0.05
G-AF	19.7	−0.02	33.80	−0.05	1.71	0.01	0.01	0.01

keeps the same underlying physical nature, e.g., the magnetic ground state, the AF/FM magnetic interaction nature, and the relative interaction strength sequence. Our results for the Ce_3Fe_8 molecule indicate that the C-AF-2 spin-ordered state has the lowest total energy, which is the ground state of the Ce_3Fe_8 molecule, different from the Ce_3Mn_8 molecule with C-AF-1 the ground state. The eight Fe ions in Ce_3Fe_8 exhibit an oxidation state of +3 with the magnetic moment of each Fe being 4.3 μ_B [35]. Some induced magnetization at the O sites is also observed similar to the Ce_3Mn_8 molecule. Each of the two Ce^{III} ions outside the Fe curb has magnetic moments of 1 μ_B, and the central Ce^{IV} has small magnetic moments (less than 0.1 μ_B). The calculations of La_3Fe_8 (see the following section) by substituting three Ce ions with trivalent cations La^{III} also confirm the oxidation state of Fe^{III} in the Ce_3Fe_8 molecule. One Fe ion in La_3Fe_8 will turn to Fe^{IV} with magnetization of 3.6 μ_B due to one less electron contribution from the La ions compared to the Ce ions.

To characterize the origin of the C-AF-2 ground state of Ce_3Fe_8, the total energies of different spin-ordered states are further analyzed by a multispin Heisenberg model [55–59] to estimate the various pairwise Fe/Fe exchange coupling parameters (J). The spin Hamiltonian is defined as

$$\hat{H} = -\sum_{i<j} J_{ij}\vec{S}_i \cdot \vec{S}_j, \tag{1}$$

where J_{ij} are magnetic coupling parameters between the Fe ions at sites i and j; $\vec{s}_i$ and $\vec{s}_j$ are the spin vectors of Fe ions at site i and j, respectively. According to Hund's rule, the five $3d$ electrons on each Fe ion should have the same spin direction, leading to a total spin of $S = 2.5$ for each Fe ion. Our total energy results indicate that four spin coupling paths exhibit significant contributions to the total energy, denoted as J_1 to J_4 in Fig. 2(b). Other coupling paths, e.g., the diagonal direction of the side faces in Fig. 2(b) (denoted as J_5), are much smaller compared to J_1 to J_4 (see Supplemental Material [54] Table S4). The calculated coupling strengths (see Table II) are $J_1 = -6.10$ meV, $J_2 = -8.11$ meV, $J_3 = -0.40$ meV, and $J_4 = +0.20$ meV (positive for FM, negative for AF). The calculated coupling strengths without SOC are also provided in Supplemental Material [54] Table S5. The strong AF interactive for $J_1 - J_3$ and weak FM interaction of J_4 results in the C-AF-2 ground state. This is completely different from the Ce_3Mn_8 molecule, in which the coupling strengths are $J_1 = +0.76$ meV, $J_2 = +0.49$ meV, $J_3 = -0.84$ meV and $J_4 = -0.18$ meV (see Supplemental Material [54] Table S3).

The detailed analyses on the different magnetic pathways were further performed to understand the underlying coupling principals in Ce_3Fe_8. The significant difference in the exchange coupling parameters between Ce_3Fe_8 and Ce_3Mn_8 is the strong AF interaction of J_1 and J_2 in Ce_3Fe_8 and weak FM interaction of J_4. Compared to Mn^{III}, Fe^{III} has one additional singly occupied $d_{x^2-y^2}$ orbital in addition to one singly occupied d_{z^2} and three singly occupied d_π orbitals. For exchange coupling parameter J_1, compared to Ce_3Mn_8, the FM interaction according to the GK rules from the two d_{z^2} orbitals meeting at a bridging O atom with the acute Mn-O-Mn angles (83°–88°) becomes weaker in Ce_3Fe_8 due to the broken Fe-O bonds, which results in a reduction of the overlap between the d_{z^2} orbitals (see Supplemental Material [54] Fig. S1). In addition, a strong AF interaction path emerges from two $d_{x^2-y^2}$ orbitals meeting at a bridging O atom with the angle of Fe-O-Fe larger than 120° in Ce_3Fe_8. This strong AF interaction path due to the singly occupied $d_{x^2-y^2}$ in the Fe ion also exists for the coupling parameter of J_2, which only has weak AF interaction due to the overlap of d_π orbitals and the superexchange through the carboxylate group (Fe-O-CR-O-Fe, R = phenyl) in Ce_3Mn_8. Therefore, a much stronger AF interaction was achieved for both J_1 and J_2 in Ce_3Fe_8. Both J_3 and J_4 involve superexchange via the carboxylate groups, which is an AF interaction. The much larger Fe-Fe distances for J_3 (4.63–4.98 Å) and J_4 (4.77–4.86 Å) compared to J_1 (3.23–3.46 Å) and J_2 (3.39–3.57 Å) pathways result in a much weaker AF interaction for J_3 and J_4. The FM interaction of J_4 contributed from the Ce-f orbitals gives rise to an overall weak FM interaction of J_4 (see the following section for details). The low-lying G-AF excited state is supported by the weak FM couplings

TABLE II. The exchange coupling parameters (J) in meV of Ce_3Fe_8, La_3Fe_8, and La_2CeFe_8. The difference of the parameters in La_3Fe_8 and La_2CeFe_8 with respect to those in Ce_3Fe_8 is shown in parentheses.

J path	Ce_3Fe_8	La_3Fe_8	La_2CeFe_8
J_1	−6.10	−6.54 (−0.44)	−6.23 (−0.13)
J_2	−8.11	−10.14 (−2.03)	−8.06 (0.05)
J_3	−0.40	−0.50 (0.1)	−0.43 (0.03)
J_4	0.20	−0.27 (−0.47)	−0.21 (−0.41)

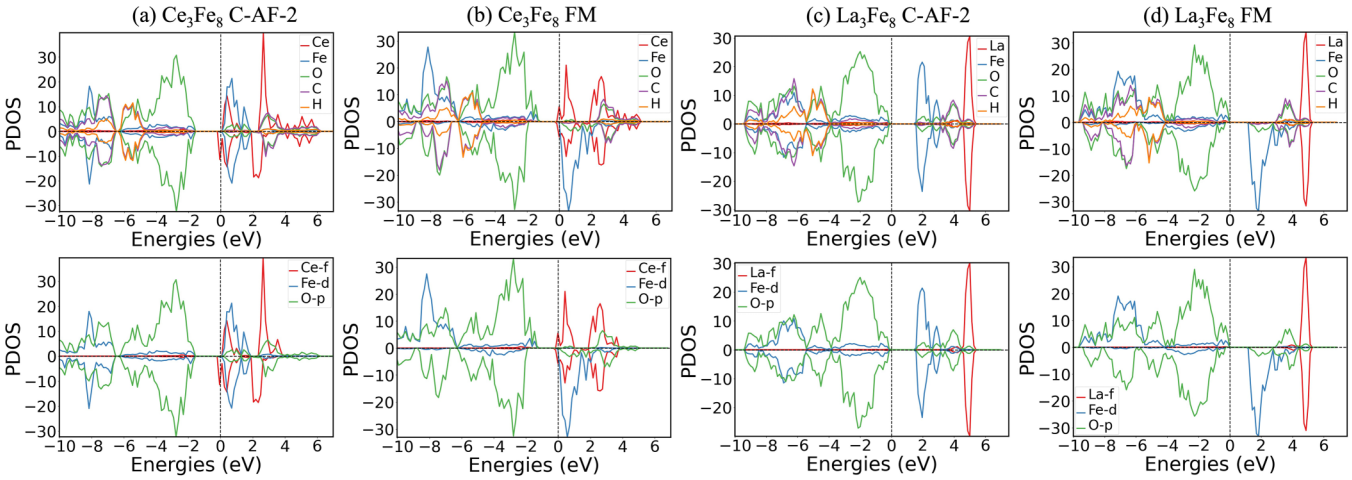

FIG. 3. The projected density of states (PDOS) using GGA+U calculations without SOC for (a) C-AF-2 and (b) FM of Ce_3Fe_8, (c) C-AF-2 and (d) FM of $[La_3Fe_8]^{-1}$. The PDOS plots in the top and bottom panels are element- and orbital-resolved, respectively.

in the c direction of J_4, corresponding to the different relative alignments of FM or AF pairs between the neighboring Fe atoms from the top and bottom Fe group, respectively.

C. Effect of Ce-f orbitals on magnetism

A direct Mn^{III}-Ce^{IV}-Mn^{III} metal-to-metal magnetic exchange channel involving the $Ce^{IV} - f$ orbitals in the Ce_3Mn_8 molecule has been reported previously [16]. The unoccupied $Ce^{IV} - f$ orbital can enhance the FM interaction leading a significant increase of the FM nature for both J_1 and J_2 in Ce_3Mn_8 compared to the La_3Mn_8 system (see Supplemental Material [54] Table S3). To reveal the role of the $Ce^{IV} - f$ orbital in Ce_3Fe_8, we similarly performed a DFT calculation for La_3Fe_8 by replacing the there Ce ions with La ions and adding an additional electron to keep the valence state of Fe ions unchanged. The projected density of state (PDOS) plots without SOC (see Fig. 3 and Supplemental Material [54] Fig. S3 for the corresponding plot with SOC) for both ground C-AF-2 and FM states show that the highest occupied molecular orbitals (HOMOs) mainly contain Fe-d and O-p orbitals for both Ce_3Fe_8 and La_3Fe_8, and the lowest unoccupied molecular orbitals (LUMOs) of Ce_3Fe_8 primarily consist of Fe-d and Ce-f orbitals, while the LUMO of La_3Fe_8 only includes Fe-d orbitals. The unoccupied La-f orbital is about 2–3 eV above LUMO, as shown in Figs. 3(c) and 3(d). As such, we built Wannier functions using Fe-d, Ce-f, and O-p orbitals for Ce_3Fe_8, while only including Fe-d and O-p orbitals for La_3Fe_8.

The calculated exchange coupling parameters J using the total energy method are listed in Table II for both Ce_3Fe_8 and La_3Fe_8. The corresponding total energies of different spin-ordering states for La_3Fe_8 are listed in Supplemental Material [54] Table S2. We found the magnetic coupling parameters of Ce_3Fe_8 have stronger FM interactions compared with La_3Fe_8. To reveal the origin of the stronger FM interactions, we first calculated the hopping terms of Ce_3Fe_8 and La_3Fe_8, which are the main contributions of the superexchange interaction [16]. The hopping terms of d_σ between Fe sites in both molecules are very similar (see Supplemental Material [54] Table S6), thus indicating that the difference in J between the two systems is caused by the difference in the FM direct exchange from the Fe-Ce-Fe interaction involving the f orbitals. However, the strengthening amount for J_2 (∼2.03 meV) is much larger than that for J_1 (∼0.44 meV) showing that the Fe-Ce-Fe FM interaction is anisotropic and directional-dependent. To understand the underlying physics, we plotted the Fe-d_σ (d_{z^2} and $d_{x^2-y^2}$) Wannier orbitals in both Ce_3Fe_8 and La_3Fe_8 systems of one site, as well as the difference between them for all eight sites, as shown in Figs. 4(a)–4(f). The Wannier functions are built in the FM configuration, in which all of the Fe ions have magnetic moments pointing in the "up" direction. The difference between the Wannier orbitals for Ce_3Fe_8 and $[La_3Fe_8]^{-1}$ reflects the influence of the Ce-f orbitals in Ce_3Fe_8. The shapes of Fe-3d Wannier orbitals have a significant effect on the direct exchanges. The significant difference among the same types of Wannier orbitals on two molecules points to the pronounced impact of the Ce-f orbitals. In particular, the effect on the Fe-d_{z^2} Wannier orbitals shows a small degree of anisotropy for J_1 and J_2 [see Fig. 4(c)], while obviously different degrees of hybridization for J_1 and J_2 can be observed from the difference of $d_{x^2-y^2}$ Wannier orbitals leading to a much stronger effect on J_2. The charge density difference plot [see Fig. 4(i)] also shows that the significant impact mainly locates in the J_2 path. This explains the stronger anisotropic behavior of the effects of Ce-f orbitals on J_1 and J_2 in Ce_3Fe_8, compared to Ce_3Mn_8, due to the extra singly occupied $d_{x^2-y^2}$ orbital in Fe ions. To reveal more details about the hybridization of $Ce^{IV} - f$ with Fe-d_σ, we plotted the PDOS of $Ce^{IV} - f$ and Fe-d_σ [see Figs. 5(a) and 5(b)] at the same energy region in which the Ce-f located. A much smaller smearing (0.01 eV) is applied in order to observe the position of the peak more precisely. The seven f orbitals are denoted as $f_{\pm3}$, $f_{\pm2}$, $f_{\pm1}$, and f_0, respectively (see the caption of Fig. 5 for details). We can clearly observe the hybridization between Fe-d_σ and Ce-f orbitals, in particular the (f_3, d_{z^2}) at 0.12 eV, 0.23 eV, and 0.68 eV, and ($f_{\pm1}$, $d_{x^2-y^2}$) at 0.40 eV. The different degree of hybridization is closed related to the shapes and positions of the orbitals, leading to a split of the seven f orbitals.

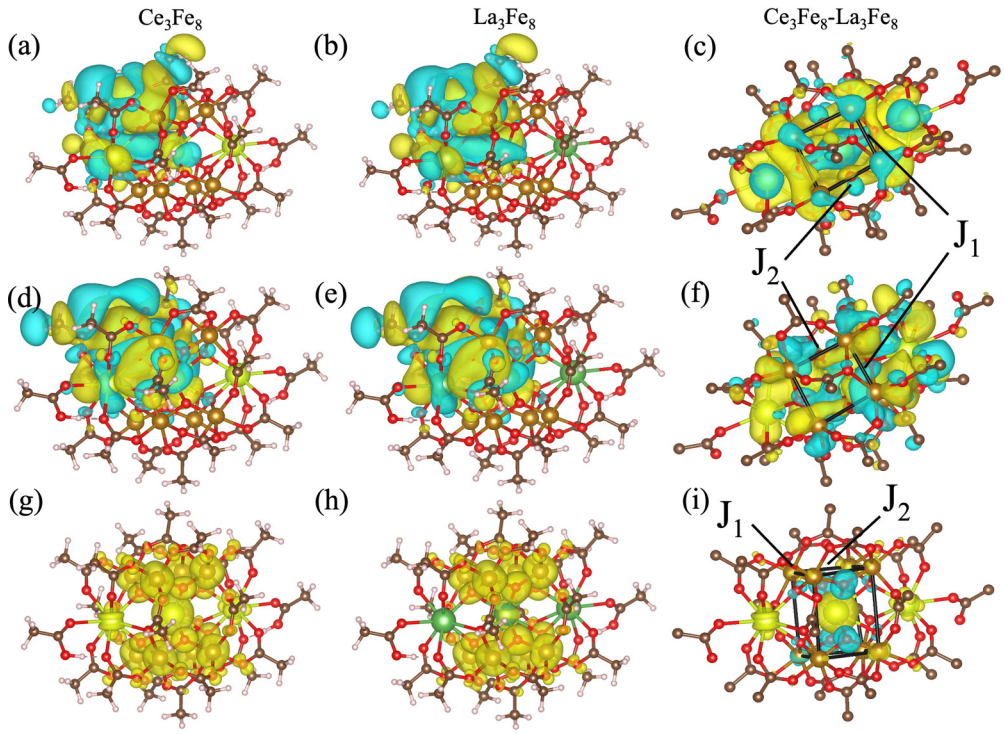

FIG. 4. Contour plots of the Wannier orbitals onto Fe-d_σ orbitals for Fe-d_{z^2} of one Fe site in (a) Ce_3Fe_8 and (b) La_3Fe_8, and (c) the difference between them for all eight Fe sites. The similar plots for Fe-$d_{x^2-y^2}$ are shown in (d), (e), and (f). The corresponding charge density and charge density difference are shown in (g), (h), and (i). Isovalues: Yellow ($4.5/\sqrt{V}$) and cyan-blue ($-4.5/\sqrt{V}$).

In addition to J_1 and J_2, the Ce-f orbitals also exhibit a strong impact on J_4 with AF interaction in La_3Fe_8 switching to FM interaction in Ce_3Fe_8, though the distance of the J_4 path is much larger than that of J_1 and J_2. In contrast, the effect of the Ce-f orbitals on J_3 is negligible. We plotted the PDOS for the Ce-f orbitals, including both the central Ce-f and the two edge Ce-f in Ce_3Fe_8, as shown in Figs. 5(c) and 5(d). Interestingly, the PDOSs of the edge Ce-f orbitals have peaks close to the Fermi level [see Fig. 5(c)], indicating a hybridization between the central Ce-f and edge Ce-f orbitals. To clarify the effects of the edge Ce-f orbitals on the magnetic exchange couplings, we additionally calculated the La_2CeFe_8 system by replacing the two edge Ce ions in Ce_3Fe_8 with La ions. The PDOS plot for the edge La-f orbitals in La_2CeFe_8 (see Fig. 5(d); the complete element- and orbital-resolved PDOSs are shown in Supplemental Material [54] Fig. S2) shows no hybridization between the central Ce-f and La-f orbitals since they are farther apart (more than 3 eV) compared to that

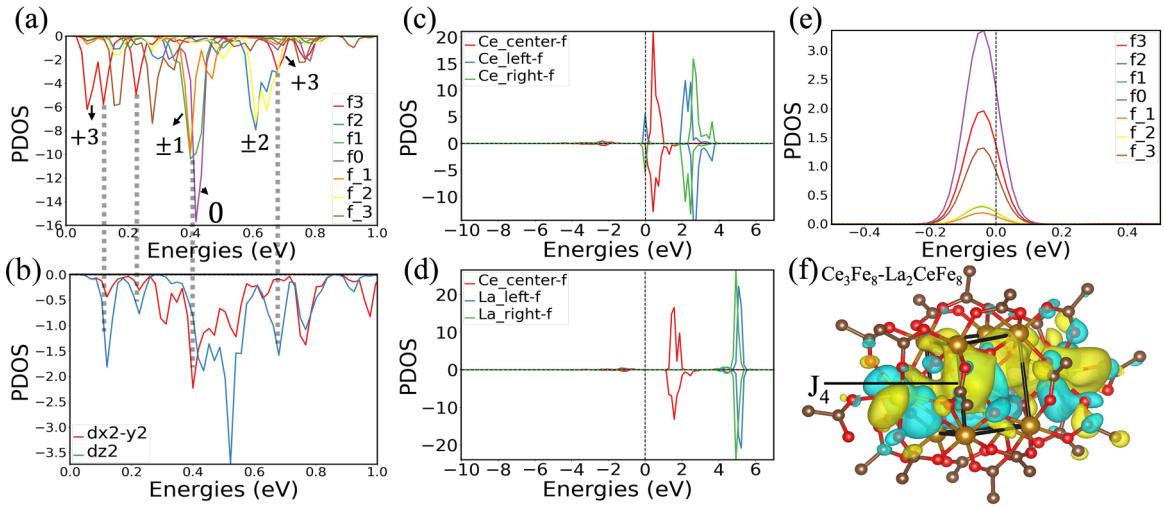

FIG. 5. The PDOS without SOC of (a) center Ce-f orbital in Ce_3Fe_8 (f_0: f_{z^3}, f_1: f_{xz^2}, f_{-1}: f_{yz^2}, f_2: f_{xyz}, f_{-2}: $f_{z(x^2-y^2)}$, f_3: $f_{x(x^2-3y^2)}$, f_{-3}: $f_{y(y^2-3x^2)}$). (b) Fe1-d_σ orbitals in Ce_3Fe_8. (c) Ce ions in Ce_3Fe_8. (d) Ce and La ions in La_2CeFe_8. (e) Left-Ce ion f orbital in Ce_3Fe_8. (f) The difference of $Ce^{IV} - f$ orbitals between Ce_3Fe_8 and La_2CeFe_8. Isovalues: Yellow ($1.5/\sqrt{V}$), cyan-blue ($-1.5/\sqrt{V}$).

between the central Ce-f and edge Ce-f in Ce_3Fe_8 (less than 2 eV). The calculated magnetic exchange parameters (J) for La_2CeFe_8 (see Table II and Supplemental Material [54] Table S2 for the corresponding energies of different spin-ordering states) show that the two edge Ce-f orbitals have little effect on $J_1 - J_3$, but exhibit significant impact on J_4 by comparing the J values with Ce_3Fe_8. Thus the effects of Ce-f orbitals on J_1 and J_2 are primarily from the central Ce-f orbital. After a close examination of the edge Ce-f PDOS peaks near the Fermi level due to the hybridization [see Fig. 5(e)], we can conclude that the edge Ce-[f_0 (f_{z^3}), f_3 ($f_{x(x^2-3y^2)}$), and f_{-3} ($f_{y(y^2-3x^2)}$)] orbitals give the main contribution to the hybridization with the central Ce-f orbitals. The projections of these three f orbitals on the plane perpendicular to the J_4 path are the largest among the seven f orbitals. The plot of the difference of Wannier orbitals to central $Ce^{IV} - f$ in Ce_3Fe_8 and La_2CeFe_8 [see Fig. 5(f)] shows a strong hybridization between the edge $Ce^{III} - f$ and central $Ce^{IV} - f$, leading to a significant change in the Ce-f Wannier orbital. This changes is mainly located on the plane along the Ce line and perpendicular to the J_4 pathway (also middle of the J_4 pathway), enhancing the Fe-Ce-Fe FM interaction for J_4 in Ce_3Fe_8, and on the other hand, a ground state of G-AF for La_2CeFe_8 due to the AF nature of J_4.

IV. DISCUSSION

We have theoretically investigated the atomic structure and electronic and magnetic properties of the molecular analog of perovskite ferrites, abbreviated as Ce_3Fe_8, using the first-principles method. In particular, we found a transition of octahedra to pentahedron in two Fe sites with disappearing JT distortion. This optimized structure is robustly stable in our simulations. We tried several initial configurations, e.g., structures with manually forced JT or no JT distortion for all eight Fe ions, the DFT optimized Ce_3Mn_8 structure by direct Fe substitutions, etc., all of which will result in the same stable structure with two FeO_5 pentahedrons after geometry optimization. We believe this structure change compared to Ce_3Mn_8 is due to the less JT-active of Fe^{III} with a local structural stress relief [60].

The contribution of the Ce-f orbital to the FM interaction was first pointed out in Ce_3Mn_8 since it located near the Fermi level [16]. Our calculation results in Ce_3Fe_8 confirm this *TM*-Ce-*TM* FM interaction and additionally identify the strong anisotropic behavior of this FM interaction due to the hybridization between Fe-$d_{x^2-y^2}$ and Ce-f orbitals. This FM interaction due to the $f - d_\sigma$ hybridization should be significantly diminished if the d_σ orbitals are unoccupied. However, for Cr-containing perovskite oxide compounds without occupied d_σ orbitals, e.g., the RCrO$_3$ family, it is reported that the FM interaction exists between Cr ions due to the *t-e* hybridization originated from the virtual charge transfer between the half-filled t_{2g} and empty e_g orbitals [61]. The f orbitals from the rear-earth elements can potentially influence the *t-e* hybridization in the corresponding molecular compounds, and thus show effects on the FM interaction. Besides, we find that the edge Ce-f orbitals located a little farther away from the Fermi level, which are omitted in previous work about Ce_3Mn_8 [16], can hybridize with the central Ce-f orbital near the Fermi level in Ce_3Fe_8, thus providing a significant contribution to the FM interaction between the neighboring TM ions of different groups (top and bottom).

The analysis above indicates that the strength of the FM *TM-d*/Ce-f/*TM-d* interaction is closely related to the shape and energy level position of the orbitals, which can be modulated by the types of cations and TM elements, as well as the molecular geometry. For example, charging the molecule can significantly change the molecular geometries and energy levels of the orbitals [18,62], thus in turn modifying the magnetic interactions within the molecules. This can induce electroresistance [62] or giant magnetocapacitance [63], and can be applied to develop multifunctional molecular-based magnetic devices, e.g., the single-molecule transistors [64]. In addition, the study on the underlying magnetism of the magnetic molecule can provide insights into the structural and physical properties of ultrasmall nanoscale perovskite materials, benefiting the use of nanoparticles in perovskite technology applications.

V. CONCLUSION

In conclusion, our investigation of the Ce_3Fe_8 magnetic molecule elaborates the complex magnetism involving both d and f orbitals at the nanoscale. The superexchange via the Fe-$d_{x^2-y^2}$ and O-p orbitals can supply a strong AF interaction for both J_1 and J_2 with relative close distance between the Fe pairs. The hybridization between the Fe-$d_{x^2-y^2}$ and central Ce-f orbitals, which contributes FM interaction, shows an anisotropic behavior for J_1 and J_2 with a much stronger FM contribution for J_2. Surprisingly, the edge Ce-f orbitals, especially the f_{z^3}, $f_{x(x^2-3y^2)}$, and $f_{y(y^2-3x^2)}$ orbitals, can interact with the central f orbitals, and thus results in a sizable FM contribution to J_4 with relative large distance between the corresponding Fe pairs. The combination of these pairwise Fe_2^{III} ferromagnetic and antiferromagnetic exchange interactions leads to a C-AF-2 spin-ordered ground state in the Ce_3Fe_8 molecule. Our work provides theoretical support for fine-tuning the magnetic properties of nanoscale molecules, e.g., by charging or structural engineering, which is a crucial strategy for future molecule-based magnetic device development.

ACKNOWLEDGMENTS

The authors would like to acknowledge financial support from the Hundreds of Talents Program of Sun Yat-sen University. The authors also acknowledge the use of computing resources from the Tianhe-2 Supercomputer.

[1] S.-W. Cheong and M. Mostovoy, Multiferroics: A magnetic twist for ferroelectricity, Nat. Mater. **6**, 13 (2007).

[2] Y. Tokunaga, N. Furukawa, H. Sakai, Y. Taguchi, T.-H. Arima, and Y. Tokura, Composite domain walls in a multiferroic perovskite ferrite, Nat. Mater. **8**, 558 (2009).

[3] R. Ramesh and N. A. Spaldin, Multiferroics: Progress and prospects in thin films, Nat. Mater. **6**, 21 (2007).

[4] Y. Tokura, Multiferroics—toward strong coupling between magnetization and polarization in a solid, J. Magn. Magn. Mater. **310**, 1145 (2007).

[5] H. Zheng, J. Wang, S. Lofland, Z. Ma, L. Mohaddes-Ardabili, T. Zhao, L. Salamanca-Riba, S. Shinde, S. Ogale, F. Bai *et al.*, Multiferroic $BaTiO_3$-$CoFe_2O_4$ nanostructures, Science **303**, 661 (2004).

[6] H. Schmid, Multi-ferroic magnetoelectrics, Ferroelectrics **162**, 317 (1994).

[7] S. Picozzi and C. Ederer, First principles studies of multiferroic materials, J. Phys.: Condens. Matter **21**, 303201 (2009).

[8] T. Ichimura, K. Fujiwara, and H. Tanaka, Dual field effects in electrolyte-gated spinel ferrite: Electrostatic carrier doping and redox reactions, Sci. Rep. **4**, 5818 (2014).

[9] L. You, F. Zheng, L. Fang, Y. Zhou, L. Z. Tan, Z. Zhang, G. Ma, D. Schmidt, A. Rusydi, L. Wang *et al.*, Enhancing ferroelectric photovoltaic effect by polar order engineering, Sci. Adv. **4**, eaat3438 (2018).

[10] W. Eerenstein, N. Mathur, and J. F. Scott, Multiferroic and magnetoelectric materials, Nature (London) **442**, 759 (2006).

[11] D. N. Hendrickson, G. Christou, W. Wernsdorfer, S. O. Hill, N. Aliaga-Alcade, S. Bhaduri, R. S. Edwards, S. M. Aubin, and Z. Sun, Half-integer spin molecular nanomagnets, MRS Online Proceedings Library **746**, 11 (2002).

[12] M. Evangelisti, A. Candini, A. Ghirri, M. Affronte, E. K. Brechin, and E. J. McInnes, Spin-enhanced magnetocaloric effect in molecular nanomagnets, Appl. Phys. Lett. **87**, 072504 (2005).

[13] W. Wernsdorfer, N. Aliaga-Alcalde, D. N. Hendrickson, and G. Christou, Exchange-biased quantum tunnelling in a supramolecular dimer of single-molecule magnets, Nature (London) **416**, 406 (2002).

[14] J. R. Friedman and M. P. Sarachik, Single-molecule nanomagnets, Annu. Rev. Condens. Matter Phys. **1**, 109 (2010).

[15] D. N. Woodruff, R. E. Winpenny, and R. A. Layfield, Lanthanide single-molecule magnets, Chem. Rev. **113**, 5110 (2013).

[16] A. E. Thuijs, X.-G. Li, Y.-P. Wang, K. A. Abboud, X.-G. Zhang, H.-P. Cheng, and G. Christou, Molecular analogue of the perovskite repeating unit and evidence for direct Mn^{III}-Ce^{IV}-Mn^{III} exchange coupling pathway, Nat. Commun. **8**, 500 (2017).

[17] D.-T. Chen, J. Chen, X.-G. Li, G. Christou, S. Hill, X.-G. Zhang, and H.-P. Cheng, Long-range magnetic exchange pathways in complex clusters from first principles, J. Phys. Chem. C **125**, 11124 (2021).

[18] Y.-P. Wang, X.-G. Li, X.-G. Zhang, G. Christou, and H.-P. Cheng, Cation substitution effect on a molecular analogue of perovskite manganites, J. Phys. Chem. C **121**, 10893 (2017).

[19] J. Varignon, M. Bibes, and A. Zunger, Origin of band gaps in 3*d* perovskite oxides, Nat. Commun. **10**, 1658 (2019).

[20] D. Sarma, N. Shanthi, S. Barman, N. Hamada, H. Sawada, and K. Terakura, Band theory for ground-state properties and excitation spectra of perovskite LaMO_3 (M = Mn, Fe, Co, Ni), Phys. Rev. Lett. **75**, 1126 (1995).

[21] F.-K. Chiang, M.-W. Chu, F. Chou, H. Jeng, H. Sheu, F. Chen, and C. Chen, Effect of Jahn-Teller distortion on magnetic ordering in Dy(Fe,Mn)O_3 perovskites, Phys. Rev. B **83**, 245105 (2011).

[22] D. M. Giaquinta and H.-C. zur Loye, Structural predictions in the ABO_3 phase diagram, Chem. Mater. **6**, 365 (1994).

[23] S. M. Ali and H. M. Al-Otaibi, The distinctive sensing performance of cobalt ion in $LaBO_3$ perovskite (B = Fe, Mn, Ni, or Cr) for hydrazine electrooxidation, J. Electroanal. Chem. **851**, 113443 (2019).

[24] T. Chakraborty, R. Yadav, S. Elizabeth, and H. Bhat, Evolution of Jahn-Teller distortion, transport and dielectric properties with doping in perovskite $NdFe_{1-x}Mn_xO_3$ ($0 \leqslant x \leqslant 1$) compounds, Phys. Chem. Chem. Phys. **18**, 5316 (2016).

[25] T. Yamaguchi, J.-P. Costes, Y. Kishima, M. Kojima, Y. Sunatsuki, N. Bréfuel, J.-P. Tuchagues, L. Vendier, and W. Wernsdorfer, Face-sharing heterotrinuclear M^{II}-Ln^{III}-M^{II} (M = Mn, Fe, Co, Zn; Ln = La, Gd, Tb, Dy) complexes: Synthesis, structures, and magnetic properties, Inorg. Chem. **49**, 9125 (2010).

[26] W. Kohn and L. J. Sham, Self-consistent equations including exchange and correlation effects, Phys. Rev. **140**, A1133 (1965).

[27] J. P. Perdew, K. Burke, and M. Ernzerhof, Generalized gradient approximation made simple, Phys. Rev. Lett. **77**, 3865 (1996).

[28] G. Kresse and J. Furthmüller, Efficiency of ab-initio total energy calculations for metals and semiconductors using a plane-wave basis set, Comput. Mater. Sci. **6**, 15 (1996).

[29] G. Kresse and J. Furthmüller, Efficient iterative schemes for *ab initio* total-energy calculations using a plane-wave basis set, Phys. Rev. B **54**, 11169 (1996).

[30] P. E. Blöchl, Projector augmented-wave method, Phys. Rev. B **50**, 17953 (1994).

[31] G. Kresse and D. Joubert, From ultrasoft pseudopotentials to the projector augmented-wave method, Phys. Rev. B **59**, 1758 (1999).

[32] S. L. Dudarev, G. A. Botton, S. Y. Savrasov, C. Humphreys, and A. P. Sutton, Electron-energy-loss spectra and the structural stability of nickel oxide: An LSDA+U study, Phys. Rev. B **57**, 1505 (1998).

[33] C. Loschen, J. Carrasco, K. M. Neyman, and F. Illas, First-principles LDA+U and GGA+U study of cerium oxides: Dependence on the effective U parameter, Phys. Rev. B **75**, 035115 (2007).

[34] J. Hong, A. Stroppa, J. Íniguez, S. Picozzi, and D. Vanderbilt, Spin-phonon coupling effects in transition-metal perovskites: A DFT+U and hybrid-functional study, Phys. Rev. B **85**, 054417 (2012).

[35] A. Abbad, W. Benstaali, H. Bentounes, S. Bentata, and Y. Benmalem, Search for half-metallic ferromagnetism in orthorhombic Ce(Fe/Cr)O_3 perovskites, Solid State Commun. **228**, 36 (2016).

[36] S. Das Gupta, R. L. Stewart, D.-T. Chen, K. A. Abboud, H.-P. Cheng, S. Hill, and G. Christou, Long-range ferromagnetic exchange interactions mediated by Mn-Ce^{IV}-Mn superexchange involving empty 4f orbitals, Inorg. Chem. **59**, 8716 (2020).

[37] K. Rushchanskii, S. Kamba, V. Goian, P. Vaněk, M. Savinov, J. Prokleška, D. Nuzhnyy, K. Knížek, F. Laufek, S. Eckel *et al.*, A multiferroic material to search for the permanent electric dipole moment of the electron, Nat. Mater. **9**, 649 (2010).

[38] S. Middey, D. Meyers, D. Doennig, M. Kareev, X. Liu, Y. Cao, Z. Yang, J. Shi, L. Gu, P. J. Ryan *et al.*, Mott electrons in an artificial graphenelike crystal of rare-earth nickelate, Phys. Rev. Lett. **116**, 056801 (2016).

[39] H. J. Zhao, L. Bellaiche, X. M. Chen, and J. Íñiguez, Improper electric polarization in simple perovskite oxides with two magnetic sublattices, Nat. Commun. **8**, 14025 (2017).

[40] F. Zuo, P. Panda, M. Kotiuga, J. Li, M. Kang, C. Mazzoli, H. Zhou, A. Barbour, S. Wilkins, B. Narayanan *et al.*, Habituation based synaptic plasticity and organismic learning in a quantum perovskite, Nat. Commun. **8**, 240 (2017).

[41] A. Shorikov, A. Lukoyanov, M. Korotin, and V. Anisimov, Magnetic state and electronic structure of the δ and α phases of metallic Pu and its compounds, Phys. Rev. B **72**, 024458 (2005).

[42] J.-P. Julien, J.-X. Zhu, and R. C. Albers, Coulomb correlation in the presence of spin-orbit coupling: Application to plutonium, Phys. Rev. B **77**, 195123 (2008).

[43] A. A. Mostofi, J. R. Yates, Y.-S. Lee, I. Souza, D. Vanderbilt, and N. Marzari, Wannier90: A tool for obtaining maximally-localised Wannier functions, Comput. Phys. Commun. **178**, 685 (2008).

[44] J. Zhang, C. Ji, J. Wang, W. Xia, X. Lu, and J. Zhu, Stabilization of *E*-type magnetic order caused by epitaxial strain in perovskite manganites, Phys. Rev. B **97**, 085124 (2018).

[45] J. Zhang, X. Lu, X. Yang, J. Wang, and J. Zhu, Origins $\uparrow\uparrow\downarrow\downarrow$ magnetic structure and ferroelectricity in multiferroic Lu_2CoMnO_6, Phys. Rev. B **93**, 075140 (2016).

[46] K. I. Kugel' and D. Khomskĭ, The Jahn-Teller effect and magnetism: Transition metal compounds, Sov. Phys. Usp. **25**, 231 (1982).

[47] J. B. Goodenough, Theory of the role of covalence in the perovskite-type manganites [La, *M*(II)]MnO_3, Phys. Rev. **100**, 564 (1955).

[48] J. B. Goodenough, An interpretation of the magnetic properties of the perovskite-type mixed crystals $La_{1-x}Sr_xCoO_{3-\lambda}$, J. Phys. Chem. Solids **6**, 287 (1958).

[49] J. Kanamori, Superexchange interaction and symmetry properties of electron orbitals, J. Phys. Chem. Solids **10**, 87 (1959).

[50] I. Shein, K. Shein, V. Kozhevnikov, and A. Ivanovskii, Band structure and the magnetic and elastic properties of $SrFeO_3$ and $LaFeO_3$ perovskites, Phys. Solid State **47**, 2082 (2005).

[51] S. Belhamra, R. Masrour, A. Jabar, and E. Hlil, A comparative study of the structural, electronic, magnetic properties and magnetocaloric effect of perovskite $LaRO_3$ (R = Mn, Cr and Fe), Polyhedron **193**, 114891 (2021).

[52] S. K. Abdel-Aal, A. E. Aly, H. M. Chanduví, A. V. G. Rebaza, E. Atteia, and A. Shankar, Magnetic and optical properties of perovskite-graphene nanocomposites $LaFeO_3$-rGO: Experimental and DFT calculations, Chem. Phys. **538**, 110874 (2020).

[53] M. Z. Hasan, M. Rasheduzzaman, and K. M. Hossain, Pressure-dependent physical properties of cubic SrBO$_3$ (B = Cr, Fe) perovskites investigated by density functional theory, Chin. Phys. B **29**, 123101 (2020).

[54] See Supplemental Material at http://link.aps.org/supplemental/10.1103/PhysRevB.108.184421 for total energy without SOC; total energy with SOC using DFT relaxed structure; the exchange coupling parameters (J) of Ce_3Mn_8 and $[La_3Mn_8]^{-1}$; exchange coupling parameters of J_5; the exchange coupling parameters (J) without SOC; hopping terms between Fe-3d_σ Wannier orbitals; −COOP analysis for bridging oxygen and Fe ions; PDOS without SOC.

[55] L. Noodleman, Valence bond description of antiferromagnetic coupling in transition metal dimers, J. Chem. Phys. **74**, 5737 (1981).

[56] L. Noodleman and E. R. Davidson, Ligand spin polarization and antiferromagnetic coupling in transition metal dimers, Chem. Phys. **109**, 131 (1986).

[57] L. Noodleman, C. Peng, D. Case, and J.-M. Mouesca, Orbital interactions, electron delocalization and spin coupling in iron-sulfur clusters, Coord. Chem. Rev. **144**, 199 (1995).

[58] K. Yamaguchi, T. Tsunekawa, Y. Toyoda, and T. Fueno, Ab initio molecular orbital calculations of effective exchange integrals between transition metal ions, Chem. Phys. Lett. **143**, 371 (1988).

[59] K. Yamaguchi, T. Fueno, N. Ueyama, A. Nakamura, and M. Ozaki, Antiferromagnetic spin couplings between iron ions in iron-sulfur clusters: A localized picture by the spin vector model, Chem. Phys. Lett. **164**, 210 (1989).

[60] S.-C. Haw, J.-M. Lee, S.-A. Chen, K.-T. Lu, M.-T. Lee, T.-W. Pi, C.-H. Lee, Z. Hu, and J.-M. Chen, Influence of Fe substitution on the Jahn-Teller distortion and orbital anisotropy in orthorhombic $Y(Mn_{1-x}Fe_x)O_3$ epitaxial films, Dalton Trans. **45**, 12393 (2016).

[61] J.-S. Zhou, J. Alonso, V. Pomjakushin, J. B. Goodenough, Y. Ren, J.-Q. Yan, and J.-G. Cheng, Intrinsic structural distortion and superexchange interaction in the orthorhombic rare-earth perovskites RCrO$_3$, Phys. Rev. B **81**, 214115 (2010).

[62] X.-G. Li, X.-G. Zhang, and H.-P. Cheng, Conformational electroresistance and hysteresis in nanoclusters, Nano Lett. **14**, 4476 (2014).

[63] Y.-N. Wu, X.-G. Zhang, and H.-P. Cheng, Giant molecular magnetocapacitance, Phys. Rev. Lett. **110**, 217205 (2013).

[64] J. Martínez-Blanco, C. Nacci, S. C. Erwin, K. Kanisawa, E. Locane, M. Thomas, F. Von Oppen, P. W. Brouwer, and S. Fölsch, Gating a single-molecule transistor with individual atoms, Nat. Phys. **11**, 640 (2015).